HHS Public Access

Author manuscript

Nat Neurosci. Author manuscript; available in PMC 2016 May 01.

Published in final edited form as:

Nat Neurosci. 2015 November ; 18(11): 1687–1697. doi:10.1038/nn.4131.

Connectivity of Mouse Somatosensory and Prefrontal Cortex Examined with Trans-synaptic Tracing

Laura A. DeNardo[#1], **Dominic S. Berns**[#1,2], **Katherine DeLoach**[1], and **Liqun Luo**[1,2]

[1]Howard Hughes Medical Institute and Department of Biology, Stanford University, Stanford, CA 94305

[2]Neurosciences Program, Stanford University, Stanford, CA 94305

[#] These authors contributed equally to this work.

Abstract

Information processing in neocortical circuits requires integrating inputs over a wide range of spatial scales, from local microcircuits to long-range cortical and subcortical connections. We used rabies virus-based trans-synaptic tracing to analyze the laminar distribution of local and long-range inputs to pyramidal neurons in the mouse barrel cortex and medial prefrontal cortex (mPFC). New findings in barrel cortex include substantial inputs from layer 3 (L3) to L6, prevalent translaminar inhibitory inputs, and long-range inputs to L2/3 or L5/6 preferentially from L2/3 or L5/6 of input cortical areas, respectively. These layer-specific input patterns are largely independent of NMDA receptor function in the recipient neurons. mPFC L5 receive proportionally more long-range inputs and more local inhibitory inputs than barrel cortex L5. These results provide new insight into the organization and development of neocortical networks and identify important differences in the circuit organization in sensory and association cortices.

The mammalian neocortex consists of discrete but interconnected functional areas that collectively encode features of the environment, form associations between stimuli, and drive behavior by transforming sensory input into motor output. Individual areas contain microcircuits that are organized vertically in columns and horizontally in layers of distinct cell types. In the rodent somatosensory cortex, barrel-related columns of cells tend to respond to stimulation of the same whisker[1, 2] and are involved in sensory perception[3]. In contrast, cortical association areas such as the prefrontal cortex regulate cognitive functions, and are not known to contain clear maps of sensory space[4].

Canonical circuits have been proposed as organizational features that are shared across sensory cortices[5-7]. In a canonical circuit model based largely on cat V1, information flows from thalamus→layer 4 (L4)→L2/3→L5/6. Mapping connectivity of the mouse barrel

Correspondence should be addressed to L.L. (lluo@stanford.edu)..

AUTHOR CONTRIBUTIONS

L.A.D., D.S.B., and L.L. designed the experiments. L.A.D. and D.S.B. performed and analyzed layer-specific trans-synaptic tracing experiments. L.A.D. performed slice recording and CRACM experiments. K.D. performed and analyzed *in situ* hybridization experiments. L.A.D., D.S.B., and L.L wrote the manuscript.

cortex largely supports the canonical circuit[8, 9]. However, the canonical circuit represents a simplified overview of prominent cortical connections and many aspects of cortical circuit organization remain unknown. What is the spatial organization of transcolumnar connectivity in cortex? What are the cellular sources of long-range input to sensory cortex? What are the developmental mechanisms that give rise to layer-specific connectivity? To what extent does the canonical circuit in sensory cortices apply to association areas?

Previous pioneering studies generated maps of local and long-range inputs to specific cortical layers, but technical limitations leave the maps incomplete. While *in vivo* dye fills allow for correlation of morphology with receptive field properties[10], synaptic connections cannot always be inferred from where dendrites and axons overlap[11]. Electrophysiological methods including paired recordings[8], glutamate uncaging[9, 12, 13], and channelrhodopsin-assisted circuit mapping (CRACM)[14, 15] enable quantification of connectivity rates and synapse strengths between defined cell types. However, paired recordings and glutamate uncaging are limited to mapping local connections within a brain slice, and CRACM can only be used to map one class of inputs at a time.

Modified rabies virus (RV) can be used to trace brain-wide monosynaptic inputs to genetically defined cell types[16, 17]. Here we used RV trans-synaptic tracing to generate layer-specific input maps to L2/3, L5, and L6 pyramidal neurons in barrel cortex. By comprehensively mapping local, inhibitory, and long-range inputs, we constructed whole-brain input maps not possible with alternative methodologies. We performed laminar analyses of inputs from barrel cortex and from other cortical regions in the sensorimotor network. To explore the developmental programs regulating layer specific cortical inputs, we coupled Cre-dependent tracing to cell-type specific knockout of the obligatory NMDA receptor subunit GluN1. Finally, we generated the first whole-brain input map to medial prefrontal cortex (mPFC) L5. Comparisons of mPFC and barrel cortex revealed differences in layer-specific microcircuit organization and in the relative contributions of inhibitory and long-range inputs to L5 neurons in each area.

RESULTS

Experimental strategy

We used RV tracing to probe the organization of inputs to excitatory neurons in L2/3, L5, and L6 of mouse barrel cortex. We injected two helper adeno-associated viruses (AAVs) that express target proteins in a Cre-dependent manner into mice where the Cre recombinase was expressed in pyramidal neurons in specific layers (**Supplementary Fig. 1a**)[18]. The first AAV (*CAG-FLEx-TVA*^{66T}*-mCherry*) expressed a mutant receptor (TVA^{66T}) for EnvA, a coat protein for an avian virus, fused with mCherry. The second AAV (*CAG-FLEx-G*) expressed RV glycoprotein (G) necessary for the trans-synaptic transport of RV. Two weeks later, we injected EnvA-pseudotyped RV in which *G* was replaced with coding sequence of GFP (RV*dG* hereafter). Because there is no cognate receptor for EnvA in the mouse brain, RV*dG* only infects TVA-expressing cells. G expression from the second AAV complements the RV*dG*, allowing retrograde monosynaptic tracing from Cre-expressing cells (**Fig. 1a**).

Starter cells expressed both mCherry and GFP, while input neurons expressed only GFP. Importantly, the mutant TVA^{66T} eliminated background labeling[18], as there was no mCherry or GFP expression in animals lacking Cre (**Supplementary Fig. 1b**). When the AAV carrying *CAG-FLEx-G* was omitted, GFP expression was predominantly restricted to cells expressing TVA^{66T}-mCherry (**Supplementary Fig. 1c**), indicating that green-only cells in experimental animals represent presynaptic partners of starter cells (inputs hereafter) due to monosynaptic spread of RV*dG*. By injecting helper AAVs into mice that received *in utero* electroporation (IUEp) of a *Cre*-expressing plasmid at E16, or into layer-specific Cre driver mice, we confined starter cells to L2/3 (IUEp-*Cre* or *SepW1^{Cre}*), L5 (*Rbp4^{Cre}*), and L6 (*Ntsr1^{Cre}*), respectively (**Fig. 1, Supplementary Fig. 1a**). We determined layer boundaries based on DAPI nuclear labeling and assigned starter cells and RV-labeled inputs to cortical layers using a custom MatLab program. Layer boundaries were consistent across Cre-drivers (**Supplementary Fig. 1d**) and with immunostaining based on layer markers Cux1 (L2–4) and Ctip2 (L5b–6) (**Supplementary Fig. 1e**).

To characterize the starter cells defined by each Cre-driver, we crossed *Rbp4^{Cre}* and *Ntsr1^{Cre}* mice to tdTomato Cre reporter mice (*Rosa^{Ai14}*); because of technical limitations (see Methods), we used Cre-dependent mCherry from AAV to characterize the *SepW1^{Cre}* expression pattern (**Supplementary Fig. 2**). Co-staining for the general neuronal marker NeuN in barrel cortex revealed that *SepW1^{Cre}* labeled ~31% of NeuN$^+$ L2/3 cells, which represents a low estimate of labeling since the viral reporter unlikely infected all L2/3 all cells (**Supplementary Fig. 2a,g**). *Rbp4^{Cre};Rosa^{Ai14}* labeled ~42% of NeuN$^+$ L5 cells (**Supplementary Fig. 2b,g**). *Ntsr1^{Cre};Rosa^{Ai14}* labeled ~68% of NeuN$^+$ cells in L6 (**Supplementary Fig. 2f,g**), consistent with previous reports[19, 20].

Layers 5b and 6 contain subcerebral and corticothalamic projection neurons, respectively[21]. We stained barrel cortex sections from *Rbp4^{Cre};Rosa^{Ai14}* mice for Ctip2, a marker for subcerebral projection neurons (SCPNs). ~50% of tdTomato$^+$ cells in L5b expressed Ctip2 (**Supplementary Fig. 2c,g**), consistent with a previous report that *Rbp4^{Cre}* labels both SCPNs and inter-telencephalic projection neurons[22]. Previous work reported that the *Ntsr1^{Cre}* line labels almost exclusively corticothalamic projection neurons in somatosensory and visual cortex L6[20, 23]. For simplicity, we use their respective layers to refer to the Cre-driver names hereafter, keeping in mind that each Cre-driver labels only a subset of cells in that layer.

A prominent L3→L6 connection in barrel cortex

We mapped mouse barrel cortex so that we could compare RV tracing to literature describing this circuitry with other methods. In addition to describing layer-specific circuits in quantitative detail, trans-synaptic tracing might uncover new or understudied connections that were disrupted in brain slices used in previous mapping studies.

We traced from layer-restricted starter cells and mapped the layer identity of labeled inputs throughout all of barrel cortex. We define these inputs (located above, below, or in a barrel visualized in L4 with DAPI staining) as local inputs hereafter. In all cases, starter cells had pyramidal morphology with apical dendrites extending towards the pia (**Fig. 1b–d**, left) and

were restricted to the layer of interest (**Fig. 1b–d**, middle; **Supplementary Table 1**). For each brain, we calculated the number of inputs in each layer as a fraction of the total inputs in barrel cortex. Starter cells in each layer received characteristic sets of inputs (**Supplementary Table 2**). L2/3 starter cells produced by IUEp-*Cre* received the largest fractions of input from L3, L4, and L5a, L5 starter cells from L3, L5a, and L5b, and L6 starter cells from L6, L5b, L3, and L4 (**Fig. 1b–d**, right; **Supplementary Table 1**). Consistent with previous work, starter cells received dense inputs from other cells within the starter cell layer[8]. Our data support the canonical pathways, including dense L4→L2/3 and L2/3→L5 connections, similar to previous reports[8, 9]. We also observed a robust input from L3→L6 in barrel cortex that was not reported in a previous paired recording study and was observed as a weak connection using glutamate uncaging[8, 9].

To validate that the L3→L6 synaptic connections are functional, we performed a CRACM experiment in which we used IUEp at E16 to express channelrhodopsin-2 fused with a fluorescent protein mVenus (ChR2-mVenus) in L2/3 of *Ntsr1*^{Cre}*;Rosa*^{Ai14} mice. One month later, we prepared acute slices and performed whole-cell patch recordings from labeled L6 cells while stimulating axons from L2/3 with a blue laser. To isolate monosynaptic excitatory postsynaptic currents (EPSCs), we voltage clamped the cells at −60 mV in the presence of tetrodotoxin (TTX), 4-aminopyridine (4-AP) and picrotoxin. In the same slices, we also recorded from L5 pyramidal cells to compare the strength of L2/3→L6 synapses to that of L2/3→L5 synapses, which are part of the canonical pathway.

In slices with robust ChR2-mVenus expression (**Fig. 1e**), 6 of 13 recorded L6 cells responded to laser stimulation with a short-latency EPSC, whereas in the same slices, 6 of 6 recorded L5 cells responded. The amplitudes of the L2/3→L6 ESPCs were ten-fold smaller than L2/3→L5 EPSCs (**Fig. 1f,g**). L2/3→L5 and L2/3→L6 EPSCs were blocked by the AMPA-type glutamate receptor antagonist 6,7-dinitroquinoxaline-2,3-dione (DNQX), indicating they were glutamate receptor-mediated (**Fig. 1h**). Since we observed few L2→L6 inputs with RV tracing (**Fig. 1d**), most of the functional connections we observed were likely L3→L6. Together, the RV tracing and CRACM results indicate that L3→L6 synapses are numerous but weak. Axons from L2/3 neurons were visible in L5 (**Fig. 1e**), suggesting that they form synapses onto distal dendrites of L6 neurons and might be subject to substantial dendritic filtering. These results highlight the utility of RV tracing in identifying connections not easily detectable with electrophysiological methods.

Spatial distribution of inputs to barrel cortex

To understand how laminar sources of input change with distance from the starter cells, we analyzed the distribution of inputs within barrel cortex along the anterior–posterior (A–P) axis (across coronal sections; **Fig. 2a**) and medial-lateral (M–L) axis (within coronal sections; **Fig. 2b**). We generated heat maps showing the average distribution across space for inputs from different layers (**Fig. 2c–h**, left). Although inputs were widely distributed, they peaked within sections containing the most starter cells. While most of the starter cells were contained within 360 μm diameter regions, inputs extended across ~2 mm of barrel cortex. Individual barrels were ~200 μm in diameter (192.2±2.3 μm, n=3 mice). Thus, while the starter cells likely occupied 2-3 barrels along one axis, the inputs occupied up to 10

barrels. Because our starter cells spanned multiple barrels and septa, we did not attempt to draw conclusions about individual barrel or septa-related circuits from our data.

We observed layer-specific differences in the distributions of inputs with distance from the starter cells. L6 inputs exhibited target-dependent spread, providing clustered input to L5 and distributed input to L6. L4 inputs clustered above or below the starter cells, while L3 and L5 inputs spread out in space (**Fig. 2c–h**, left). To quantify differences along the A–P axis, we identified sections that contained 95% of the starter cells (central sections, **Fig. 2a**) and compared the layer distribution of those inputs to the distribution of inputs in peripheral sections (**Fig. 2c–e** right). For the M–L axis, we focused on the central sections, and determined the distance from each input or starter cell to a center line projected through the middle of the labeled cells (**Fig. 2b**). We defined a middle region that contained 95% of the starter cells in these sections and compared the layer distribution of inputs located in the middle and flanking side regions (**Fig. 2f–h**, right). L4 inputs to L2/3 and L5 significantly decreased along the A–P and M–L axes, respectively (**Fig. 2c,g**). L6 received significantly smaller fractions of L4 with distance along both axes (**Fig. 2e,h**).

Overall, the laminar distribution of input varied predictably with distance from the starter cell population, with L4 neurons providing less relative input from distant locations to starter cells in all layers. Consistent with previous reports of axon arborization patterns[24], these data suggest that L4 primarily conveys intracolumnar information, while supra- and infragranular layers also convey information from adjacent barrels. Given that different classes of L6 neurons have unique intracortical axon patterns[25], the target-dependent spread of L6 inputs might reflect input from different cell types within L6.

Patterns of GABAergic inputs to barrel cortex

Inhibition plays an important role in shaping receptive fields and determining the timing of neuronal responses[26]. To identify whether RV-labeled inputs were excitatory or inhibitory, we performed *in situ* hybridization using a mixture of probes that detect mRNAs for the GABA synthetic enzymes glutamic acid decarboxylase 1 and 2 (*Gad1/2*) on $SepW1^{Cre}$, $Rbp4^{Cre}$, *and* $Ntsr1^{Cre}$ brains with layer-specific RV tracing in L2/3, L5, and L6, respectively. $SepW1^{Cre}$ became available during the course of our study. Since this line specifically labeled L2/3 neurons and yielded input patterns indistinguishable from the inputs to cells labeled with IUEp (no significant differences by t-tests with Holm-Sidak corrections for multiple comparisons), we used $SepW1^{Cre}$ driver for these experiments.

We quantified the number of Gad^{+} inputs in starter cell-containing sections (**Fig. 3a**). Starter cells were largely restricted to the layer of interest (**Fig. 3b–d**, **Supplementary Table 3**) and the distribution of inhibitory inputs reflected the overall patterns of input, with a bias toward the same layer as the starter cells (**Fig. 3e–j**; **Supplementary Table 3**). GABAergic cells constituted 15%, 9.8%, and 9.5% of total inputs within counted sections to L2/3, 5, and 6 starter cells, respectively; the fraction of inputs that were GABAergic within each layer further differed for different starter cell populations (**Fig. 3k–m**). We observed a prevalence of inhibitory neurons in L1 and prominent intralaminar inhibition, consistent

with previous reports[14, 27]. We also observed large fractions of translaminar inhibition, especially from L2/3→L5 and L5→L2/3.

We examined the spatial spread of both *Gad*$^{-}$ and *Gad*$^{+}$ inputs to each layer along the M–L axis of barrel cortex in central sections. While starter cells occupied 300–400 μm, *Gad*$^{-}$ (presumed excitatory) inputs spread throughout ~2 mm of cortex and maintained an hourglass shape with constriction in L4 (**Supplementary Fig. 3**, upper panels). *Gad*$^{+}$ inputs were more clustered than *Gad*$^{-}$ inputs, spanning ~1 mm of cortical space around the starter cells (**Supplementary Fig. 3**, lower panels), suggesting that excitatory and inhibitory inputs to the same starter cells span approximately 10 and 5 barrel columns, respectively. *Gad*$^{+}$ inputs exhibited the most spread in the starter layer, indicating that the most lateral inhibition derives from the starter layer.

Long-range layer-specific input to barrel cortex

Barrel cortex is reciprocally connected with motor cortices, non-barrel-related S1 ($S1_{body}$), and S2 in sensorimotor processing circuits[13, 28-30], but little is known about the laminar identity of long-range inputs to specific layers of barrel cortex. We observed numerous long-range inputs from $S1_{body}$, S2, M1, and M2 (**Fig. 4a–d**), from which we derived the first maps of projections from individual layers of M1, M2, $S1_{body}$, and S2 to individual layers of barrel cortex. We also observed prominent input from ventral posteromedial (VPM) and posteromedial (POm) thalamic nuclei to L2/3, L5, and L6 (**Fig. 4c, 4e–g**), consistent with previous findings that L4 is not the only layer that receives thalamic input[31-34].

Compared to barrel cortex inputs, $S1_{body}$ and S2 provided fewer inputs from L5 to L2/3, while $S1_{body}$ and S2 inputs to L5 and L6 more closely resembled the local input patterns (**Fig. 1b-d, 4h-m**). Long-range inputs to L2/3, L5, and L6 of barrel cortex came from progressively deeper layers, respectively. This pattern was most striking between barrel cortex and M1; while barrel cortex L2/3 received M1 inputs from L2-5b (**Fig. 4n**) and L5 received M1 inputs from L2-L6 (**Fig. 4o**), L6 received M1 inputs almost exclusively from L5b-L6 (**Fig. 4p**). M2 inputs to L5 and L6 originated mostly from L5 (**Fig. 4q–r**). Generally, superficial layers of barrel cortex received more long-range cortical input from superficial layers, whereas deep layers received more long-range cortical input from deep layers, suggesting distinct routes of information flow in feedback pathways.

Testing the role of NMDA receptors in shaping connectivity

Activity plays a key role in circuit development [35-40], but little is known about its role in layer-specific synapse formation. By coupling coincident pre- and post-synaptic activity to calcium signaling, the NMDA receptor implements activity-dependent changes in wiring during development[36]. To examine whether activity sculpted input distributions, we traced inputs to neurons lacking GluN1, the obligatory subunit of NMDA receptors. We crossed layer-specific Cre lines to a conditional *GluN1* allele (*GluN1*^{fl}) and a *GluN1* null allele (*GluN1*$^{\Delta}$) to remove GluN1 from Cre-active cells (*Cre; GluN1*$^{fl/\Delta}$), a subset of which were starter cells for RV tracing (**Fig. 5a**). For L2/3 input tracing, Cre was electroporated *in utero* at E16 (**Supplementary Fig. 1a**). In both *Rbp4*^{Cre} and *Ntsr1*^{Cre} driver mice, Cre reporter

expression was detected by P1 (**Supplementary Fig. 1a**), suggesting that *GluN1* was deleted well before the peak of cortical synaptogenesis around P14[41, 42].

To confirm that GluN1 was removed from Cre-expressing $GluN1^{fl/\Delta}$ cells, we recorded synaptic currents from TVA^{66T}-mCherry-labeled cells in $Ntsr1^{Cre};GluN1^{fl/+}$ and $Ntsr1^{Cre};GluN1^{fl/\Delta}$ mice. $GluN1^{fl/+}$ cells had robust GluA- and GluN-mediated EPSCs (**Fig. 5b, left**). In contrast, $GluN1^{fl/\Delta}$ cells had robust GluA-mediated EPSCs at −60 mV, but significantly reduced GluN-mediated EPSCs at +40 mV (**Fig. 5b– d**). In $GluN1^{fl/\Delta}$ cells, DNQX suppressed the EPSCs observed at +40 mV, indicating that they were GluA-mediated, while control cells maintained 20% of the EPSC at +40 mV after DNQX wash-in, indicating that much of that EPSC was GluN-mediated (**Supplementary Fig. 4**).

We compared the pattern of input to GluN1-lacking and control starter cells (control data in **Fig. 1,4**). Cortical layer thicknesses were similar between conditions (**Supplementary Fig. 5a–d**), as were the patterns of input to GluN1-lacking L2/3, L5, and L6 starter cells (**Fig. 5e–m, Supplementary Table 4**), except for a significant increase in the fraction of L6→L5 inputs (**Fig. 5j**) and a significant decrease in the fraction of L6→L6 inputs for GluN1-lacking starter cells (**Fig. 5m**). We found no changes in the fractional distribution of long-range input to L5 and L6 from cortical areas and thalamus (**Supplementary Fig. 5e,f**). The laminar distribution of inputs was also similar for control and GluN1-lacking starter cells (**Supplementary Fig. 5e,f**) except that GluN1-lacking L5 starter cells received significantly more input from S2 L6 (**Supplementary Fig. 5e**).

Thus, eliminating GluN1 signaling had minimal effects on patterns of input, with the exception of particular connections involving deep layer neurons. These loss-of-function data suggest that NMDA receptors within L6 neurons normally promote the formation or maintenance of recurrent connections from other L6 neurons, while NMDA receptors in L5 normally inhibit formation or maintenance of L6 inputs from barrel cortex and S2.

Comparing local input to mPFC and barrel cortex L5

We next tested whether layer-specific connectivity patterns in sensory cortex also apply to association cortex. Of the Cre lines we used for layer-specific input mapping in barrel cortex, only $Rpb4^{Cre}$ maintains layer specificity in mPFC. We traced the inputs to L5 cells in mPFC and compared the results to barrel cortex. To characterize the potential starter cells in mPFC L5, we immunostained mPFC sections from $Rbp4^{Cre};Rosa^{Ai14}$ mice with antibodies against NeuN or Ctip2 (**Supplementary Fig. 2d,e**). $Rbp4^{Cre};Rosa^{Ai14}$ labeled ~46% of $NeuN^{+}$ L5 cells and 51% of $tdTomato^{+}$ cells in L5b expressed Ctip2, similar to what we observed in barrel cortex (**Supplementary Fig. 2g**).

mPFC starter cells were located in infralimbic (IL) and prelimbic (PL) cortex (**Fig. 6a**) in L5a and L5b with a small fraction in L3 (**Fig. 6b, Supplementary Table 5**). Layers were assigned based on DAPI staining for each section and were consistent with layer boundaries based on expression of Cux1 (L3) and Ctip2 (L5b/6) (**Supplementary Fig. 6a–b**, see Methods). Control experiments revealed minimal local background (**Supplementary Fig. 6c–d**). Inputs were distributed throughout all layers, with the largest fraction from L5a and L5b (**Fig. 6c, Supplementary Table 5**). Since mPFC lacks a detectable L4, we removed L4

inputs from our barrel cortex analysis to simplify the comparison. Compared to barrel cortex, mPFC L5 cells received a greater fraction of input from L1, L5b and L6 at the expense of L3 (**Fig. 6c**). Since L3 is thinner and L5 is thicker in mPFC than in barrel cortex (**Supplementary Fig. 6b, Supplementary Fig. 1d**), layer thickness could contribute to these differences. After normalizing input distribution by layer thickness, L5 cells in mPFC still received significantly more L1 input at the expense of L3, but the fractional input from L5 was comparable (**Supplementary Fig. 6e**). Thus, while layer thickness may explain the fractional differences in L5 recurrent connectivity, it alone cannot account for the distinct patterns of translaminar input between barrel cortex and mPFC.

We also analyzed the distribution of local inputs along the A–P and dorsal-ventral (D–V) axes. As in barrel cortex (**Fig. 2**), starter cells were contained within 360 μm diameter regions of mPFC; inputs peaked within sections that contained the most starter cells but also extended across ~2 mm of mPFC (**Fig. 6d–e**). While we observed trends suggesting that L5 inputs spread more with distance compared to inputs from other layers of mPFC, these trends did not reach significance when we compared the fraction of inputs by layer in central versus peripheral (**Fig. 6d**) and middle versus side regions (**Fig. 6e**).

To characterize the local GABAergic inputs to mPFC L5 cells, we performed *Gad1/2 in situ* hybridization on sections containing starter cells (**Fig. 6f–g**). Similar to barrel cortex, we observed that the pattern of inhibition in mPFC reflected the overall pattern of input with a slight bias towards inputs from L5 (**Fig. 6h**). The percent of inhibitory input was relatively consistent across layers, ranging from 18-27% (**Fig. 6i**). Interestingly, there was a 2.5–fold increase in the GABAergic fraction of local inputs to mPFC L5 cells compared to barrel cortex L5 (**Fig. 6j**), indicating that ratio of local excitatory to inhibitory inputs to L5 pyramidal cells varies between cortical areas.

mPFC L5 receives proportionally more long-range input

mPFC and barrel cortex L5 cells received drastically different fractional inputs from local versus long-range areas. Whereas barrel cortex L5 cells received on average 79% of their total inputs from other cells in ipsilateral barrel cortex, mPFC L5 cells only received 21% of their inputs from other ipsilateral mPFC cells (**Fig. 6k**). This could be because barrel cortex is approximately twice the volume of mPFC (barrel cortex per hemisphere = 4.1±0.4 mm^3, n=5 mice; mPFC per hemisphere = 1.9±0.02 mm^3, n=4 mice). However, most of the inputs within barrel cortex and mPFC were located within 1 mm of the starter cells (**Fig. 2d,g; 6d,e**), suggesting the volumes containing local inputs in each area were similar. Alternatively, the local connection probability could vary by region.

To determine if the spread of inputs to L5 starter cells differs between barrel cortex and mPFC, we plotted the local fraction of total inputs along the A–P (**Fig. 6l**) and D–V (**Fig. 6m**; M–L for barrel cortex) axes for each area. We did not observe significant differences in the fraction of local inputs at sites distant (360-1,080 μm) from starter cells, suggesting mPFC and barrel cortex starter cells receive local inputs from similar volumes of cortical space. However, we observed significantly smaller fractions of inputs to mPFC L5 at sites close to the starter cells along both axes (**Fig. 6l,m**). This was not due to a reduced number

of potential inputs, as the density of neurons in mPFC and barrel cortex was similar (**Fig. 6n**). Thus, the decreased fraction of local input to mPFC compared to barrel cortex is not due to differences in cortical size or available inputs, but instead may reflect distinct local connection probabilities between the two areas.

Major long-range inputs to L5 mPFC neurons originated from other prefrontal areas including agranular insula (AI, **Fig. 7a**), from the dorsal polymodal thalamic nuclei (~26%, **Fig. 7b**), contralateral mPFC (cPFC, ~11%; **Fig. 7c**), motor areas (~5%, **Fig. 7d**), with more minor inputs from claustrum (CLA, **Fig. 7e**), CA1 cells throughout the dorsal–ventral axis of the hippocampus (**Fig. 7f**), and the basolateral amygdala (BLA, **Fig. 7g,h**). Local mPFC inputs mPFC came about equally from IL and PL (**Fig. 7i**). Within the dorsal thalamus, we observed inputs from the medial (MED), midline (MTN), anterior (ANT), intralaminar (ILM), and lateral (LAT) groups, with MED and ANT each contributing approximately 10% of the overall inputs to L5 (**Fig. 7j**). The anterior cingulate area (ACA) was the major source of PFC input, contributing about 10% of the total inputs to mPFC L5 with smaller contributions from agranular insula, orbital (ORB), tenia tecta (TTd), and the dorsal peduncular area (DP) (**Fig. 7k**), and cPFC contributed ~11% of the overall input (**Fig. 7l**). Dorsal sensory thalamus (**Fig. 7m**) and motor cortex (MC) (**Fig. 7n**) each contributed 5% of the overall input. Finally, mPFC L5 cells received smaller fractions of input from the medial septal complex (MSC, **Fig. 7o**), sensory and association cortices (**Fig. 7p**), and various hypothalamic nuclei (**Fig. 7q**). These data are largely consistent with classical retrograde tracer studies that mapped inputs to mPFC[43]. Here we demonstrate that neurons from these regions provide monosynaptic input directly onto L5 pyramidal neurons. In contrast to barrel cortex, which is a dedicated circuit for processing sensorimotor information, mPFC circuits integrate information from diverse brain regions involved in a wide variety of cognitive functions and behaviors.

Furthermore, the large fraction of local inhibitory inputs in mPFC (**Fig. 6j**) likely participate in feedforward inhibitory circuits driven by long-range inputs such that the local inhibition reflects the overall excitatory drive to L5 cells in a given cortical area rather than scaling with the number of local excitatory inputs.

DISCUSSION

We used RV trans-synaptic tracing to generate local and long-range input maps to genetically defined pyramidal cells in L2/3, L5, and L6 of the mouse barrel cortex and to mPFC L5 (**Fig. 8**, see **Supplementary Fig. 7** for raw numbers). While a powerful tool to visualize the distribution of inputs to specific neuronal populations, RV tracing does not label all inputs and lacks information about the strength of labeled connections. If RV tracing is biased towards certain connections, the relative input maps may not accurately represent overall connectivity. We are not aware of such biases, but this potential caveat should be kept in mind while interpreting our results. On the other hand, RV tracing labels connections in intact tissue and has the potential to identify many connections that are not easily detected in slice recordings or glutamate uncaging, including long-range connections from cortical areas and subcortical inputs. The Cre-lines we used here allowed us to trace from a mixed population of L5 neurons (*Rbp4*^{Cre}) and a relatively pure population of L6

cortico-thalamic neurons (*Ntsr1*^{Cre}). Using additional Cre-lines with unique cell-type specificity or tracing inputs to functionally defined cell types will further expand our understanding of cortical circuit organization. Ultimately, the combination of anatomy-based studies such as RV tracing with functional connectivity data will be required to understand more completely the contributions of different connections to cortical information processing.

Our RV-based layer-specific input map identified cortical pathways that have been described with other methods, as well as prominent L3→L6 connections (**Fig. 1d, 8a**) that were not apparent in electrophysiological studies in brain slices[8, 9]. CRACM confirmed that L3→L6 connections are functional but weak compared to L3→L5 connections (**Fig. 1e–h**). Compared to somatic recordings, RV tracing may be more sensitive in detecting weak synaptic connections. Consistent with this notion, a recent RV trans-synaptic tracing study observed substantial L2/3→L6 connections in V1[44] whereas an electrophysiological mapping study reported sparse and weak connections from L2/3→L6 in V1[45]. It will be important to assess how these weak connections interact at the level of the dendrite as they could powerfully impact on the output of the cell through supralinear interactions with simultaneously active synapses or back-propagating action potentials[46].

We observed a preferential superficial→superficial and deep→deep layer connectivity structure between motor and barrel cortices, with inputs to layer 6 particularly biased towards deep layers (**Fig. 8c**). Motor cortex is strongly activated prior to and during whisking, and it sends information about self-generated movements back to barrel cortex. It will be interesting to test whether layer-specific pathways carry different kinds of information about exploratory whisking, for example.

The mutant TVA receptor we used, while reducing Cre-independent, non-specific labeling to zero (**Supplementary Fig. 1**), may preferentially reduce the efficiency of long-range input tracing[18]. Thus, the fraction of long-range input we reported is likely an underestimate. Nevertheless, the relative laminar distribution of long-range input should still be informative, as should be the comparison between barrel cortex and mPFC (**Fig. 8a,b,d,e**). We observed that mPFC L5 cells receive a much larger fraction of their total input from long-range sources. mPFC L5 cells also received a significantly larger fraction of local inhibitory inputs than barrel cortex, suggesting that many mPFC inhibitory cells participate in feedforward inhibitory circuits driven by long-range inputs[47]. Thus, the large local fraction of inhibitory inputs to mPFC L5 neurons may participate in diverse inhibitory microcircuits recruited by different behaviorally-relevant long-range inputs.

Removing NMDAR activity from starter cells revealed that NMDARs may preferentially influence a subset of connections originating from L6 neurons (**Fig. 8a, 8c**), potentially related to the activity-dependence of L6 axon targeting seen during visual cortex development[37]. Our data also indicate that the distribution of long-range inputs and the layer specificity of cortical inputs are largely independent of the presence of NMDARs in the starter cells. Our results contrast with the critical role that NMDAR activity plays in determining connectivity onto reelin-expressing interneurons[48], and suggest that NMDARs differentially regulate circuit development in distinct cortical cell types.

While RV tracing can reveal information about labeled presynaptic partners including morphology, transmitter phenotype, and position within cortex, it may not detect changes in synaptic strength or functional specificity, such as preferential connectivity for neurons with similar tuning properties[49], which may require NMDAR activity. Our starter cells were not confined to individual barrels, so subtle effects influencing connectivity within and between barrels may also be beyond our detection limit, but the overall pattern of layer-specific connections is largely independent of NMDAR, and by extension, correlated neuronal activity. Thus molecular determinants likely play a large role in layer-specific cortical connectivity. Our strategy of RV tracing in combination with layer-specific knockout of genes provides a means to test candidate molecular determinants in the future.

METHODS

Mice

All animal procedures followed animal care guidelines approved by Stanford University's Administrative Panel on Laboratory Animal Care (APLAC). Both male and female mice from mixed CD1 and C57/Bl6 backgrounds were used. Mice were group housed. *SepW1*^{Cre} mice[22] were obtained from the National Institutes of Health, *Rbp4*^{Cre} and *Ntsr1*^{Cre} mice[50] were obtained from the MMRRC, *GluN1*$^{fl/fl}$ mice[51] and Cre-dependent tdTomato reporter *Rosa*^{Ai14} mice[52] were obtained from the Jackson Laboratories. To characterize Cre drivers, *Rbp4*^{Cre} *and Ntsr1*^{Cre} were crossed to *Rosa*^{Ai14} mice (**Supplementary Fig. 2**). While *SepW1*^{Cre} allowed us to generate L2/3-restricted starter cells at P21 (**Fig. 3**), crossing *SepW1*^{Cre} to *Rosa*^{Ai14} mice resulted in tdTomato labeling throughout the entire brain (data not shown), suggesting that *SepW1*^{Cre} is active in most cells early in development and becomes layer restricted with age. Thus, to characterize L2/3 cells defined by *SepW1*^{Cre}, we injected large volumes of AAV *(CAG-FLEx-TVA*^{66T}*-mCherry)* into barrel cortex at P25 and analyzed the expression pattern at P40. The *GluN1*$^{\Delta}$ allele was generated by crossing *GluN1*$^{fl/fl}$ to a germline Cre (*hprt*^{Cre}). To study the effect of GluN1 knockout in L2/3, we crossed *GluN1*$^{fl/fl}$ to *GluN1*$^{\Delta/+}$ mice and performed *in utero* electroporation of a Cre-expressing plasmid at E16. To study the effects of *GluN1* knockout in L5 and L6, we generated *Rbp4*^{Cre}*;GluN1*$^{\Delta/+}$ and *Ntsr1*^{Cre}*;GluN1*$^{\Delta/+}$ mice, respectively, and crossed them to *GluN1*$^{fl/fl}$ mice. *GluN1*$^{fl/+}$ mice were combined with *GluN1*$^{+/+}$ mice in the control group for all analyses.

DNA constructs

DNAs encoding Cre-2A-BFP-3x Myc were subcloned in frame into the pCAG vector. Briefly, pCAG was digested with BsrG1 and EcoR1 and Cre and 2A-BFP-3x myc fragments were subcloned in simultaneously using an InFusion kit (Clontech).

In utero electroporation

Timed-pregnant mice (E16) were anaesthetized with 3% isoflurane and given preoperative injection of Buprenex at 0.05-0.1 mg/kg. The abdomen was swabbed with iodine. A small vertical incision was made in the skin and abdominal wall and embryos were gently exposed. Each embryo was injected with 1–2 μl of DNA solution and 0.01% Fast Green using a pressure-controlled glass pipette. After each injection, the embryos were moistened

with PBS and voltage steps via tweezertrodes (BTX, 5 mm round, platinum, BTX electroporator) were applied at a 45° angle with respect to the interaural line to target barrel cortex. Voltage was 36 V for five 50 ms pulses at 1 Hz as described previously[53]. The embryos were returned to the abdomen, which was sutured, followed by suturing of the skin. The procedure typically lasted 20 min.

Viral procedures

AAV vectors containing *CAG-FLEx-G* (2×10^{11} genomic copies (GC)/mL) and *CAG-FLEx-TVA^{66T}-mCherr* (1×10^{12} GC/mL) were described previously[18] and produced by the UNC viral vector core. EnvA-pseduotyped RV*dG* (1×10^{10} IU/mL) was produced in-house based on established procedures[54]. For trans-synaptic labeling, 0.1 µl of 1:1 mixture of AAV2 or AAV8 *CAG-FLEx-G* and AAV2 *CAG-FLEx-TVA^{66T}-mCherry* was injected into the brain at postnatal day (P) 21 by using a stereotactic apparatus (KOPF). During surgery, animals were anesthetized with 65 mg/kg ketamine and 13 mg/kg xylazine (Lloid Laboratories). For barrel cortex injections, the pipette was placed 0.25 mm posterior and 3.1 mm lateral from the bregma and 0.25 or 0.4 mm from the brain surface to target L2/3 or L5, respectively, or 0.7 mm posterior and 3.5 mm lateral from bregma and 0.85 mm from the brain surface for L6. For mPFC injections, the needle was placed 1.8 mm anterior, 0.3 mm lateral, and 2.5 mm deep from bregma. After recovery, animals were housed in regular 12 hr dark/light cycle with food and water ad libitum. Two weeks later, 0.5 µl of EnvA-pseudotyped RV*dG* was injected into the same brain location under anesthesia. After recovery, animals were housed in a biosafety room for 5 days to allow RV*dG* infection, trans-synaptic spread, and expression of sufficient amount of GFP to label presynaptic cells.

Histology

Animals were perfused transcardially with phosphate buffered saline (PBS) followed by 4% paraformaldehyde (PFA). Brains were dissected, post-fixed in 4% PFA for 12–24 hours, and placed in 30% sucrose for 24–48 hours. They were then embedded in Optimum Cutting Temperature (OCT, Tissue Tek) and stored at −80°C until sectioning. 60 µm floating sections were collected into PBS. For Cre line characterization and layer analysis, sections were incubated in 0.3% PBST and 10% donkey serum for 1 hour and then stained with mouse anti-NeuN (Millipore MAB377, 1:1,000), rat anti–Ctip2 (Abcam ab18465, 1:200), or rabbit anti-Cux1 (Santa Cruz SC-13024, 1:500) for 1–4 nights at 4°C in 0.3% PBST and 5% donkey serum. All sections washed 3×10 min in PBS and additionally stained with NeuroTrace Blue (1:1,000) in 0.3% PBST for 2 hours, followed by DAPI (1:10,000 of 5 mg/mL, Sigma-Aldrich) in PBS for 10–15 min, and then washed once more with PBS prior to mounting onto Superfrost Plus slides and coverslipping with Fluorogel (Electron Microscopy Sciences). The sections were imaged at 5× using a Leica Ariol Slide Scanner microscope with an SL200 slide loader, and scanner images were processed with custom software[55].

In situ hybridization

Gad1 and *Gad2* ISH probes were prepared and hybridized in *SepW1^{Cre}* (L2/3), *Rbp4^{Cre}* (L5) and *Ntsr1^{Cre}* (L6) trans-synaptic tracing brains as previously described[55]. 5-7 starter

cell containing sections were analyzed per brain. Images were collected on a Zeiss 780 confocal microscope.

Electrophysiology

At P28, the brain was removed and placed in ice-cold carbogenated slicing artificial cerebrospinal fluid (ACSF) that contains (in mM) 83 NaCl, 2.5 KCl, 1 NaH_2PO_4, 26.2 $NaHCO_3$, 22 glucose, 72 sucrose, 0.5 $CaCl_2$, and 3.3 $MgSO_4$. We cut 300 μm coronal sections on a Leica vibratome. Slices were allowed to recover at 31°C for 40 min and then at room temperature for 30 min to 6 hr. Slices were then placed in carbogenated recording ACSF (119 NaCl, 2.5 KCl, 26 $NaHCO_3$, 1 NaH_2PO_4, 1.5 $MgSO_4$, 2.5 $CaCl_2$, and 11 glucose, all in mM) that contained 50 μM picrotoxin (Sigma). For CRACM experiments, TTX (Tocris, 1 μM) and 4-AP (Sigma, 100 μM) were also included in the recording solution. Signals were recorded with a 5× gain, low-pass filtered at 2 kHz, digitized at 10 kHz (Molecular Devices Multiclamp 700B), and analyzed with pClamp 10 (Molecular Devices). Whole-cell recordings were made using 3–5 MΩ pipettes filled with an internal solution that contained (in mM) 123 Cs-gluconate, 8 NaCl, 1 $CaCl_2$, 10 EGTA, 10 HEPES, and 10 glucose, pH 7.3 with CsOH, 280–290 mOsm. Series resistance (R_s) and input resistance (R_{in}) were monitored throughout the experiment by measuring the capacitive transient and steady-state deflection, respectively, in response to a −5 mV test pulse. Responses were evoked by stimulating the white matter with a platinum 2–contact cluster electrode (FHC) 100-200 μm lateral to the recording site, or for CRACM experiments, by photostimulating $ChR2^+$ axon terminals with an optical fiber coupled to a diode-pumped solid-state 473 laser positioned ~300 μm from the recording site. Cells were clamped at −60 mV to measure GluA (AMPA-receptor)-mediated excitatory postsynaptic currents (EPSC) and then at +40 mV to measure a compound EPSC that was quantified at 50 ms after stimulus onset, at which point the GluA-mediated currents had largely decayed. Analysis was based on the average of 10 sweeps. mCherry and tdTomato-positive L6 cells were visually identified based on red fluorescence (Olympus BX51WI).

Data analysis

Regions were identified based on DAPI and NeuroTrace signal with reference to an atlas[56]. Barrel cortex was identified based on the presence of L4 barrels visible with nuclear stains. $S1_{body}$ was adjacent to barrel cortex and had a thick L4 but lacked barrel structures. Similarly, S2 was identified adjacent and ventral to $S1_{body}$ based on the reference atlas. M1 and M2 were identified based on their location as defined by the reference atlas, and characterized by the disappearance of L4 and expansion of L5. M2 was flanked by the cingulate area on the medial side, and M1 was flanked by $S1_{body}$ on the lateral side[57]. Finally, thalamic nuclei were defined based on the reference atlas with aid from nuclear stains. Dorsal polymodal thalamus groups were defined based on the Allen Reference Atlas (Allen Institute for Brain Science, 2014, http://mouse.brain-map.org/).

Data was analyzed using custom MatLab software (code available from the authors upon request). All GFP-labeled cells were clicked by the user. Section order was maintained during tissue processing and imaging, so each cell had coordinates specifying the anterior–posterior position within the brain, and the precise location within that section. For each

section, the pial surface of the region of interest was outlined, and the lower boundary of each layer was identified based on differences in the density of DAPI staining. The distance-to-pia for every cell was calculated based on its coordinates, and layer identity was assigned by comparing this distance to the defined layer boundaries. To boost confidence in our layer-assignments, we stained BC and mPFC sections for neuronal markers for L2/3/4 (Cux1) and 5b/6 (Ctip2) and calculated layer boundaries based on marker expression patterns. In both areas, DAPI-based layer assignments were consistent with neuronal marker-based assignments (**Supplementary Fig. 1b, 6a**).

To generate A–P heat maps, inputs were combined into 120 μm bins, and divided by the total cells in barrel cortex. Distributions were aligned between animals on the bin with the most starter cells. The M–L analysis was limited to the sections that contained 95% of the starter cells. The median center of mass for inputs in each layer was calculated within each section, and the center line was projected through the centers of mass. Distance-to-center was measured for every cell as the minimum distance to the center line, and given a sign to indicate medial or lateral direction from center. Distances were combined across sections within each animal. Middle cells were defined as those with distances-to-center within the range containing 95% of the starter cells. Side cells were those with distances-to-center outside this range. To generate the M–L heat maps, cells were combined into 120 μm bins centered on the center line, and combined across sections within each animal. Cell counts for each bin were divided by the total number of cells in the sections analyzed, and fractions for each bin were averaged across animals. A–P and M–L heat maps both show the average fraction of cells per bin across all animals. D–V heat maps for mPFC were generated identically to the M–L heat maps. Statistics and graphing were performed using Prism software (GraphPad). Data was analyzed blind to genotype. Brains with inefficient tracing (<100 inputs), or major tissue damage were excluded from analysis.

Statistical analyses

A supplementary methods checklist is available summarizing statistical tests and results. Data randomization was not applicable to our study, and no statistical methods were used to predetermine sample sizes but our sample sizes are similar to those reported in previous publications.[18] Data distributions were assumed to be normal but were not formally tested. When performing multiple t-tests, statistical significance was determined using the Holm-Sidak method, with alpha=5%. Each row was analyzed individually, without assuming a consistent SD. All t-tests were two-sided. For a complete list of statistical tests and p-values, see **Supplementary Table 6**.

Supplementary Material

Refer to Web version on PubMed Central for supplementary material.

ACKNOWLEDGEMENTS

We thank K. Miyamichi for critical discussions while designing experiments, the Luo lab and K. Svoboda for helpful comments on the manuscript, P. Joshi and S. McConnell for *Rbp4*^{Cre} and *Ntsr1*^{Cre} mice, and C. Gerfen for *SepW1*^{Cre} mice. L.L is an investigator of the Howard Hughes Medical Institute. This work was supported by NIH grants T32NS007280-27 and F32NS087860 (L.A.D.), F31DC013240 (D.S.B.), and R01-NS050835 (L.L.).

REFERENCES

1. Woolsey TA, Van der Loos H. The structural organization of layer IV in the somatosensory region (SI) of mouse cerebral cortex. The description of a cortical field composed of discrete cytoarchitectonic units. Brain Res. 1970; 17:205–242. [PubMed: 4904874]
2. Simons DJ. Response properties of vibrissa units in rat SI somatosensory neocortex. J Neurophysiol. 1978; 41:798–820. [PubMed: 660231]
3. Guo ZV, et al. Flow of cortical activity underlying a tactile decision in mice. Neuron. 2014; 81:179–194. [PubMed: 24361077]
4. Fuster, JM. The prefrontal cortex : anatomy, physiology, and neuropsychology of the frontal lobe. Academic Press; Philadelphia: 2008.
5. Douglas RJM, Martin KAC, Whitteridge D. A Canonical Microcircuit for the Neocortex. Neural Computation. 1989; 1:480–488.
6. Thomson AM, Lamy C. Functional maps of neocortical local circuitry. Front Neurosci. 2007; 1:19–42. [PubMed: 18982117]
7. Douglas RJ, Martin KA. Neuronal circuits of the neocortex. Annu Rev Neurosci. 2004; 27:419–451. [PubMed: 15217339]
8. Lefort S, Tomm C, Floyd Sarria JC, Petersen CC. The excitatory neuronal network of the C2 barrel column in mouse primary somatosensory cortex. Neuron. 2009; 61:301–316. [PubMed: 19186171]
9. Hooks BM, et al. Laminar analysis of excitatory local circuits in vibrissal motor and sensory cortical areas. PLoS Biol. 2011; 9:e1000572. [PubMed: 21245906]
10. Gilbert CD, Wiesel TN. Morphology and intracortical projections of functionally characterised neurones in the cat visual cortex. Nature. 1979; 280:120–125. [PubMed: 552600]
11. Brown SP, Hestrin S. Intracortical circuits of pyramidal neurons reflect their long-range axonal targets. Nature. 2009; 457:1133–1136. [PubMed: 19151698]
12. Callaway EM, Katz LC. Photostimulation using caged glutamate reveals functional circuitry in living brain slices. Proc Natl Acad Sci U S A. 1993; 90:7661–7665. [PubMed: 7689225]
13. Hooks BM, et al. Organization of cortical and thalamic input to pyramidal neurons in mouse motor cortex. J Neurosci. 2013; 33:748–760. [PubMed: 23303952]
14. Katzel D, Zemelman BV, Buetfering C, Wolfel M, Miesenbock G. The columnar and laminar organization of inhibitory connections to neocortical excitatory cells. Nat Neurosci. 2011; 14:100–107. [PubMed: 21076426]
15. Petreanu L, Huber D, Sobczyk A, Svoboda K. Channelrhodopsin-2-assisted circuit mapping of long-range callosal projections. Nat Neurosci. 2007; 10:663–668. [PubMed: 17435752]
16. Wickersham IR, et al. Monosynaptic restriction of transsynaptic tracing from single, genetically targeted neurons. Neuron. 2007; 53:639–647. [PubMed: 17329205]
17. Callaway EM, Luo L. Monosynaptic Circuit Tracing with Glycoprotein-Deleted Rabies Viruses. J Neurosci. 2015; 35:8979–8985. [PubMed: 26085623]
18. Miyamichi K, et al. Dissecting local circuits: parvalbumin interneurons underlie broad feedback control of olfactory bulb output. Neuron. 2013; 80:1232–1245. [PubMed: 24239125]
19. Olsen SR, Bortone DS, Adesnik H, Scanziani M. Gain control by layer six in cortical circuits of vision. Nature. 2012; 483:47–52. [PubMed: 22367547]
20. Kim J, Matney CJ, Blankenship A, Hestrin S, Brown SP. Layer 6 corticothalamic neurons activate a cortical output layer, layer 5a. J Neurosci. 2014; 34:9656–9664. [PubMed: 25031405]
21. Greig LC, Woodworth MB, Galazo MJ, Padmanabhan H, Macklis JD. Molecular logic of neocortical projection neuron specification, development and diversity. Nat Rev Neurosci. 2013; 14:755–769. [PubMed: 24105342]
22. Gerfen CR, Paletzki R, Heintz N. GENSAT BAC cre-recombinase driver lines to study the functional organization of cerebral cortical and basal ganglia circuits. Neuron. 2013; 80:1368–1383. [PubMed: 24360541]
23. Bortone DS, Olsen SR, Scanziani M. Translaminar inhibitory cells recruited by layer 6 corticothalamic neurons suppress visual cortex. Neuron. 2014; 82:474–485. [PubMed: 24656931]

24. Feldmeyer D. Excitatory neuronal connectivity in the barrel cortex. Front Neuroanat. 2012; 6:24. [PubMed: 22798946]
25. Zhang ZW, Deschenes M. Intracortical axonal projections of lamina VI cells of the primary somatosensory cortex in the rat: a single-cell labeling study. J Neurosci. 1997; 17:6365–6379. [PubMed: 9236245]
26. Isaacson JS, Scanziani M. How inhibition shapes cortical activity. Neuron. 2011; 72:231–243. [PubMed: 22017986]
27. Li J, Schwark HD. Distribution and proportions of GABA-immunoreactive neurons in cat primary somatosensory cortex. J Comp Neurol. 1994; 343:353–361. [PubMed: 7517965]
28. Welker E, Hoogland PV, Van der Loos H. Organization of feedback and feedforward projections of the barrel cortex: a PHA-L study in the mouse. Exp Brain Res. 1988; 73:411–435. [PubMed: 3215316]
29. Porter LL, White EL. Afferent and efferent pathways of the vibrissal region of primary motor cortex in the mouse. J Comp Neurol. 1983; 214:279–289. [PubMed: 6853758]
30. Mao T, et al. Long-range neuronal circuits underlying the interaction between sensory and motor cortex. Neuron. 2011; 72:111–123. [PubMed: 21982373]
31. Constantinople CM, Bruno RM. Deep cortical layers are activated directly by thalamus. Science. 2013; 340:1591–1594. [PubMed: 23812718]
32. Wimmer VC, Bruno RM, de Kock CP, Kuner T, Sakmann B. Dimensions of a projection column and architecture of VPM and POm axons in rat vibrissal cortex. Cereb Cortex. 2010; 20:2265–2276. [PubMed: 20453248]
33. Beierlein M, Connors BW. Short-term dynamics of thalamocortical and intracortical synapses onto layer 6 neurons in neocortex. J Neurophysiol. 2002; 88:1924–1932. [PubMed: 12364518]
34. Viaene AN, Petrof I, Sherman SM. Synaptic properties of thalamic input to layers 2/3 and 4 of primary somatosensory and auditory cortices. J Neurophysiol. 2011; 105:279–292. [PubMed: 21047937]
35. Katz LC, Shatz CJ. Synaptic activity and the construction of cortical circuits. Science. 1996; 274:1133–1138. [PubMed: 8895456]
36. Bi G, Poo M. Synaptic modification by correlated activity: Hebb's postulate revisited. Annu Rev Neurosci. 2001; 24:139–166. [PubMed: 11283308]
37. Dantzker JL, Callaway EM. The development of local, layer-specific visual cortical axons in the absence of extrinsic influences and intrinsic activity. J Neurosci. 1998; 18:4145–4154. [PubMed: 9592094]
38. Datwani A, Iwasato T, Itohara S, Erzurumlu RS. NMDA receptor-dependent pattern transfer from afferents to postsynaptic cells and dendritic differentiation in the barrel cortex. Mol Cell Neurosci. 2002; 21:477–492. [PubMed: 12498788]
39. Espinosa JS, Wheeler DG, Tsien RW, Luo L. Uncoupling dendrite growth and patterning: single-cell knockout analysis of NMDA receptor 2B. Neuron. 2009; 62:205–217. [PubMed: 19409266]
40. Iwasato T, et al. Cortex-restricted disruption of NMDAR1 impairs neuronal patterns in the barrel cortex. Nature. 2000; 406:726–731. [PubMed: 10963597]
41. De Felipe J, Marco P, Fairen A, Jones EG. Inhibitory synaptogenesis in mouse somatosensory cortex. Cereb Cortex. 1997; 7:619–634. [PubMed: 9373018]
42. White EL, Weinfeld L, Lev DL. A survey of morphogenesis during the early postnatal period in PMBSF barrels of mouse SmI cortex with emphasis on barrel D4. Somatosens Mot Res. 1997; 14:34–55. [PubMed: 9241727]
43. Hoover WB, Vertes RP. Anatomical analysis of afferent projections to the medial prefrontal cortex in the rat. Brain Struct Funct. 2007; 212:149–179. [PubMed: 17717690]
44. Velez-Fort M, et al. The stimulus selectivity and connectivity of layer six principal cells reveals cortical microcircuits underlying visual processing. Neuron. 2014; 83:1431–1443. [PubMed: 25175879]
45. Zarrinpar A, Callaway EM. Local connections to specific types of layer 6 neurons in the rat visual cortex. J Neurophysiol. 2006; 95:1751–1761. [PubMed: 16319201]

46. London M, Hausser M. Dendritic computation. Annu Rev Neurosci. 2005; 28:503–532. [PubMed: 16033324]
47. Dilgen J, Tejeda HA, O'Donnell P. Amygdala inputs drive feedforward inhibition in the medial prefrontal cortex. J Neurophysiol. 2013; 110:221–229. [PubMed: 23657281]
48. De Marco Garcia NV, Priya R, Tuncdemir SN, Fishell G, Karayannis T. Sensory inputs control the integration of neurogliaform interneurons into cortical circuits. Nat Neurosci. 2015; 18:393–401. [PubMed: 25664912]
49. Ko H, et al. Functional specificity of local synaptic connections in neocortical networks. Nature. 2011; 473:87–91. [PubMed: 21478872]
50. Gong S, et al. Targeting Cre recombinase to specific neuron populations with bacterial artificial chromosome constructs. J Neurosci. 2007; 27:9817–9823. [PubMed: 17855595]
51. Tsien JZ, Huerta PT, Tonegawa S. The essential role of hippocampal CA1 NMDA receptor-dependent synaptic plasticity in spatial memory. Cell. 1996; 87:1327–1338. [PubMed: 8980238]
52. Madisen L, et al. A robust and high-throughput Cre reporting and characterization system for the whole mouse brain. Nat Neurosci. 2010; 13:133–140. [PubMed: 20023653]
53. Navarro-Quiroga I, Chittajallu R, Gallo V, Haydar TF. Long-term, selective gene expression in developing and adult hippocampal pyramidal neurons using focal in utero electroporation. J Neurosci. 2007; 27:5007–5011. [PubMed: 17494686]
54. Osakada F, Callaway EM. Design and generation of recombinant rabies virus vectors. Nat Protoc. 2013; 8:1583–1601. [PubMed: 23887178]
55. Weissbourd B, et al. Presynaptic partners of dorsal raphe serotonergic and GABAergic neurons. Neuron. 2014; 83:645–662. [PubMed: 25102560]
56. Paxinos, G.; Franklin, KBJ. The Mouse Brain in Stereotaxic Coordinates, Second Edition. Academic Press; 2001.
57. Brecht M, et al. Organization of rat vibrissa motor cortex and adjacent areas according to cytoarchitectonics, microstimulation, and intracellular stimulation of identified cells. J Comp Neurol. 2004; 479:360–373. [PubMed: 15514982]

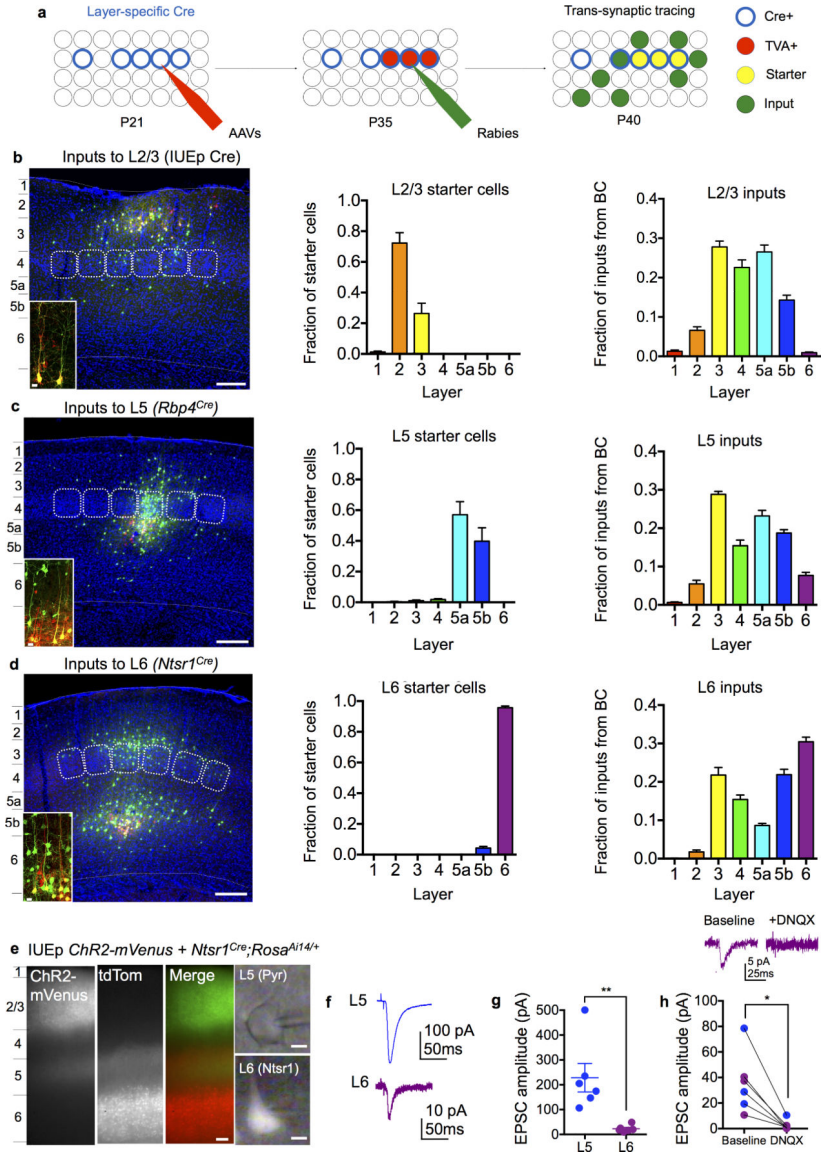

Figure 1.

Layer-specific input tracing in mouse barrel cortex. **(a)** Experimental design and timeline of layer-specific RV tracing. **(b–d)** Layer-specific tracing in barrel cortex. Left, representative coronal sections showing local tracing (insets: confocal images of starter cells). Starter cells (SCs, Middle) and local input (Right) distributions are quantified according to cortical layers for SCs in L2/3 (**b**: SCs, 76±27; total Inputs, 1,148±340; n=6 mice), L5 (**c**: SCs, 84±27; total Inputs, 1,677±359; n=9 mice), and L6 (**d**: SCs, 117±42; total Inputs, 1,751±542; n=9 mice). Scale bars represent 200 μm or 20 μm (insets). See Supplementary Table 1 for numerical values, and Supplementary Fig. 1 for controls for RV tracing. **(e–h)** L3→L6 CRACM. **(e)** Example coronal sections from an *Ntsr1*^{Cre};*Rosa*^{Ai14} mouse expressing ChR2-mVenus in L2/3. Right: recorded L5 pyramidal (pyr) and tdTomato+ L6 cell (Ntsr1). Scale bars represent 100 μm (left panels) and 10 μm (zoomed panels, right). **(f)** Traces from a L5 and L6 cell following laser stimulation of ChR2-expressing L3 axons in the presence of TTX, 4-

AP, and PTX. **(g)** Evoked EPSC amplitudes in L5 and L6 (L5: 205.2±57.48 pA, n=6 cells; L6: 23.05±5.50 pA, n=6 cells from 3 mice; p=0.0052, Student's t-test). **(h)** Representative trace (top) and quantification (bottom) of blockade of light-evoked EPSC following bath DNQX application (Baseline: 35.89±2.64 pA, DNQX: 2.64±1.61 pA, n=6 cells from 3 mice, p=0.01, paired t-test). All summary statistics are presented as mean±SEM. See Supplementary Table 6 for test results and p-values.

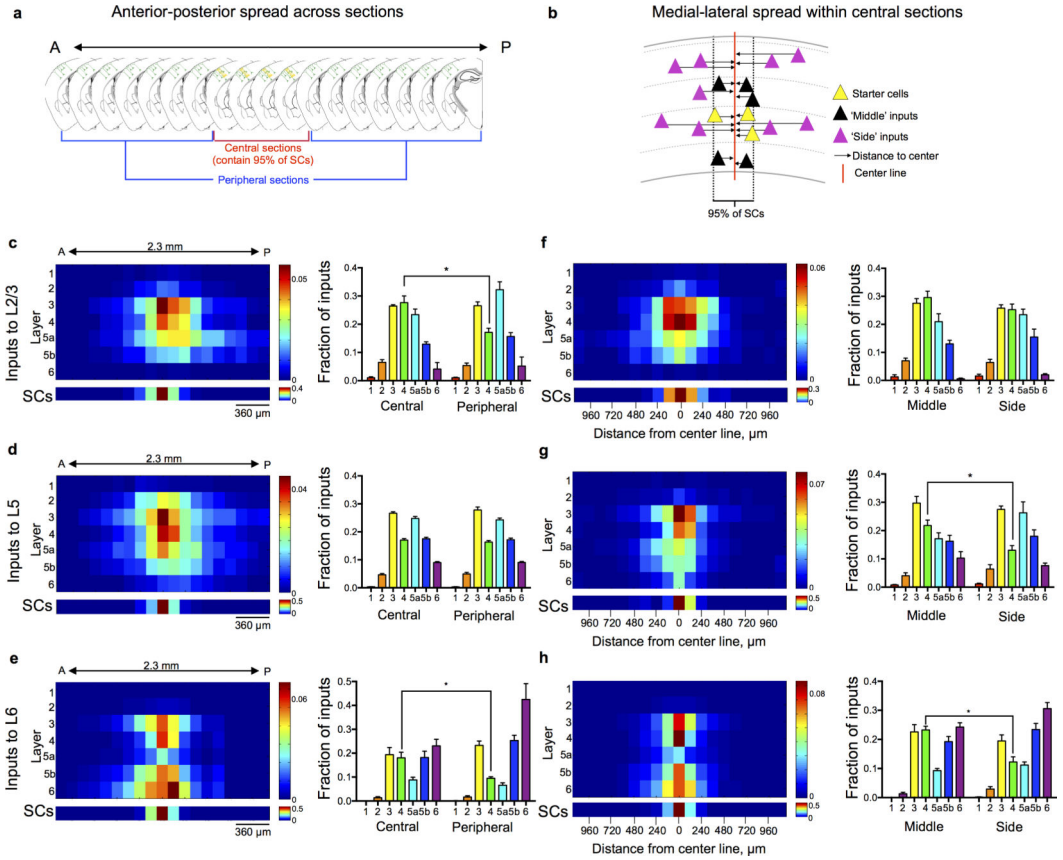

Figure 2.

Spatial analyses of synaptic inputs from barrel cortex to starter cells in L2/3, L5, and L6. **(a)** Schematic of fractional analysis of inputs along the A–P axis. **(b)** Schematic of fractional analysis of inputs along M–L axis in the central sections. **(c–e)** Left, heat maps of distribution of starter cells (SCs, lower panels) and inputs (upper panels) along the A–P axis for inputs to L2/3 (n=6 mice), to L5 (n=9 mice), and to L6 (n=9 mice). Colors represent fraction of total barrel cortex inputs according to the index at right. Bin widths are 120 µm. Right, fraction of inputs in central versus peripheral sections. **(f–h)** Left, heat maps of distribution of starter cells (SCs, lower panels) and inputs (upper panels) along the M–L axis for inputs to L2/3 (n=5 mice), to L5 (n=6 mice), and to L6 (n=9 mice). Colors represent fraction of barrel cortex inputs within the sections analyzed. Bin widths are 120 µm. Right, quantification of fraction of inputs in middle versus side regions. * denotes significant p-values from multiple t-tests with Holm-Sidak correction for multiple comparisons (α=0.05). Summary statistics presented as mean±SEM. See Supplementary Table 6 for test results and p-values.

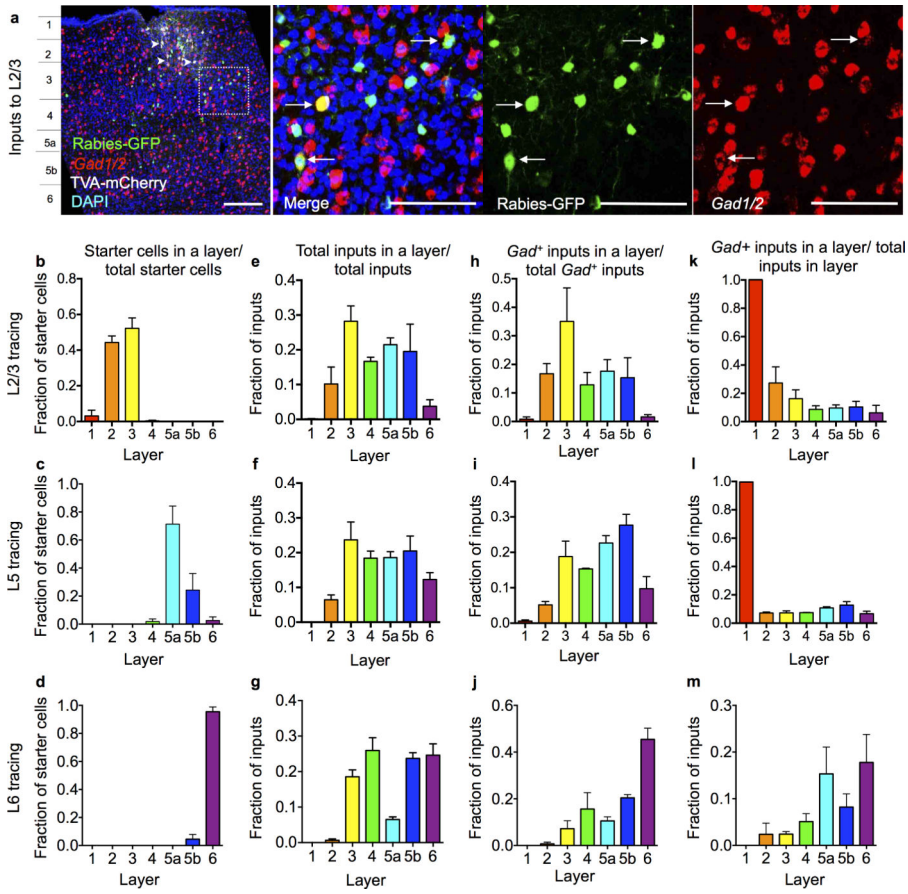

Figure 3.

Analysis of local inhibitory inputs to starter cells in L2/3, L5, and L6. **(a)** Representative coronal sections of RV tracing to L2/3 in a *SepW1*^{Cre} mouse combined with *Gad1/2 in situ* hybridization. Inhibitory inputs are double-positive for GFP (green) and *Gad1/2* (red) and are labeled with arrows. Starter cells are double-positive for GFP (green) and mCherry (white) and a subset are indicated with arrowheads. Excitatory inputs are green-only. Scale bar represents 200 μm (1st panel) or 100 μm (2nd–4th panels, magnified from the dashed box in the 1st panel). **(b–d)** Starter cells are mostly restricted to the defined layer (L2/3 SCs: 48±19, n=3 mice; L5 SCs: 16±2, n=3 mice; L6 SCs: 95±6, n=3 mice). **(e–g)** Fraction of input (*Gad*$^{+}$ and *Gad*$^{-}$) within sections on which *Gad1/2 in situ* hybridization was performed (L2/3 total inputs: 342±154, n=3 mice; L5 total inputs: 983±173, n=3 mice; L6 total inputs: 605±184, n=3 mice). **(h–j)** Inhibitory inputs are distributed throughout all layers in a pattern that was specific to the layer origin of starter cells (L2/3 *Gad*$^{+}$ inputs: 91±16, n=3 mice; L5 *Gad*$^{+}$ inputs: 34±7, n=3 mice; L6 *Gad*$^{+}$ inputs: 52±16, n=3 mice). **(k–m)** Inhibitory inputs occupy specific fractions of inputs within each layer. Summary statistics presented as mean±SEM. See Supplementary Table 3 for numerical values).

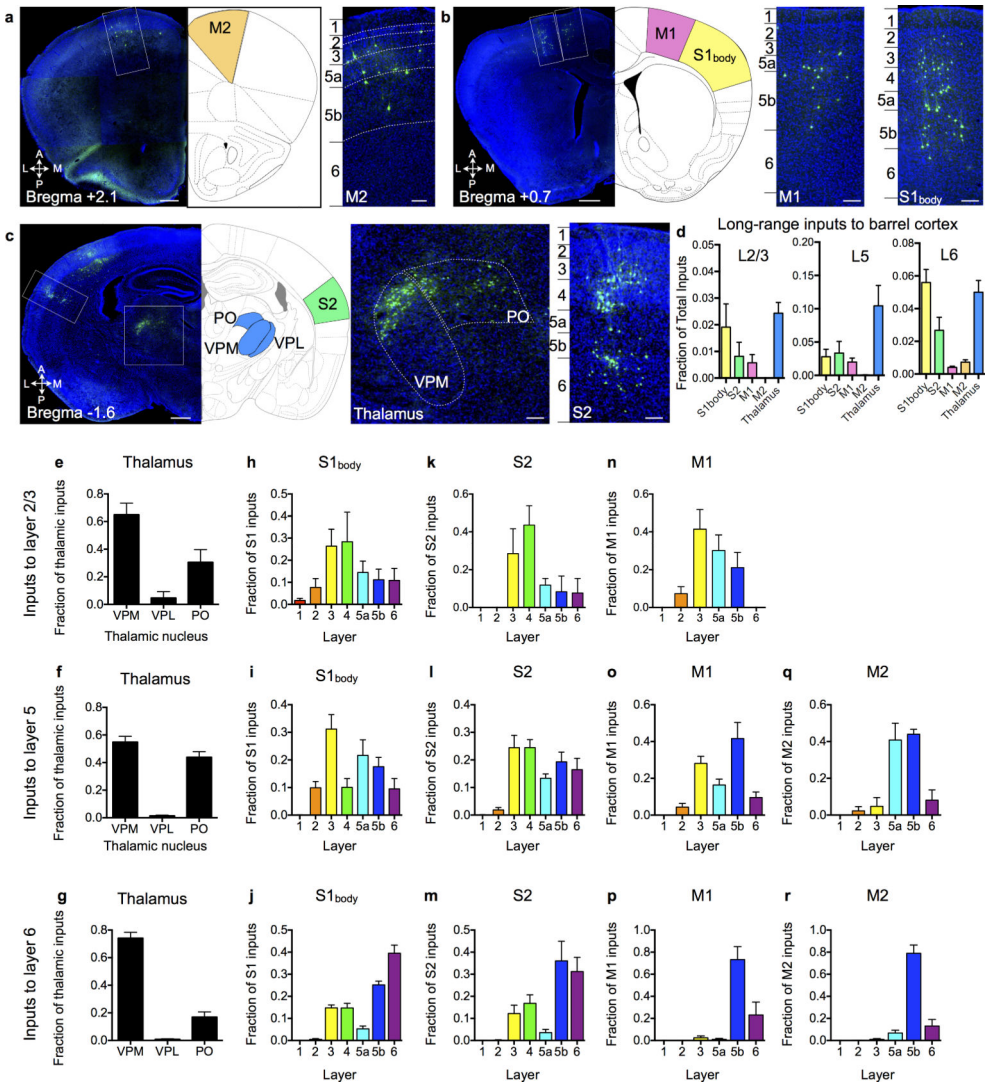

Figure 4.

Laminar analyses of long-range inputs to starter cells in L2/3, L5, and L6. **(a–c)** Atlas locations and example images showing long-range inputs to barrel cortex L5 from **(a)** secondary motor cortex (M2), **(b)** primary motor cortex (M1), primary somatosensory cortex ($S1_{body}$), **(c)** somatosensory thalamus (VPM/POm) and secondary somatosensory cortex (S2). Scale bars represent 500 μm (hemisection images), or 100 μm (zoomed images). **(d)** Quantification of fraction of total inputs contributed by each area. **(e–r)** Regional analysis of thalamic inputs (e–g) and laminar analysis of long-range inputs to L2/3 (n=6 mice), L5 (n=9 mice), and L6 (n=9 mice) from $S1_{body}$ (h–j), S2 (k–m), M1 (n–p), and M2 (q–r). Summary statistics presented as mean±SEM. Schematics are modified from Paxinos and Franklin, 2001.

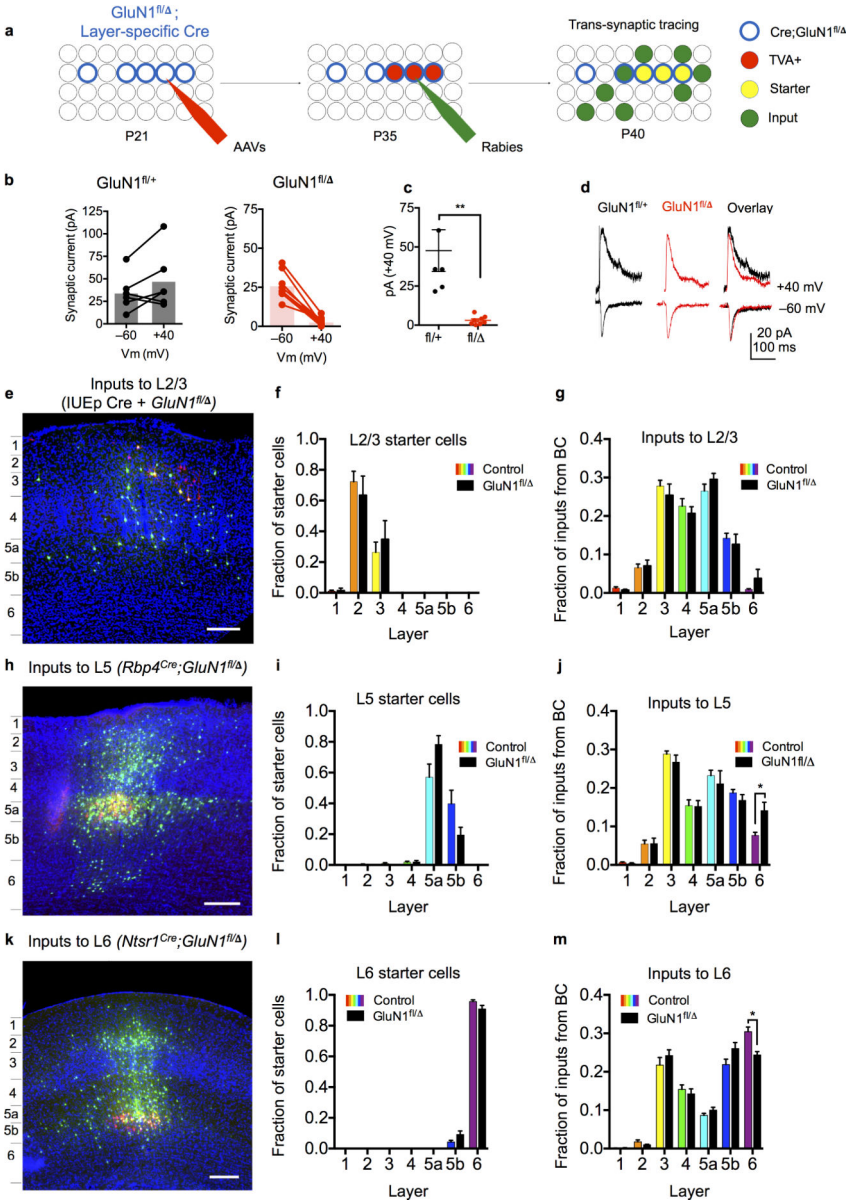

Figure 5.

Layer-specific tracing from starter cells lacking GluN1. **(a)** Experimental design. RV tracing was performed as described in Fig. 1, except on mice in which starter cells (as well as other Cre-expressing cells in the starter cell layer, blue circles) lacked GluN1. **(b–d)** Electrophysiological characterization of *GluN1* mutant cells. **(b)** Synaptic currents measured in $Ntsr1^{Cre};GluN1^{fl/+}$ (heterozygous control, left: −60 mV: 34.6±8.4 pA; +40 mV: 47.7±13.3 pA, n=6 cells from 2 mice) and $Ntsr1^{Cre};GluN1^{fl/\Delta}$ (mutant, right: −60 mV: 26.2±3.1 pA; +40 mV: 3.1±1.0 pA, n=8 cells from 2 mice). **(c)** Quantification of NMDA synaptic current in heterozygous control (black) and mutant (red) (fl/+: 47.69±13.33 pA, n=6 cells from 2 mice; fl/Δ: 3.07±0.97 pA, n=8 cells from 2 mice, p=0.002, Student's t test). **(d)** Example recordings from $Ntsr1^{Cre};GluN1^{fl/+}$ (black) and $Ntsr1^{Cre};GluN1^{fl/\Delta}$ (red) cells. **(e, h, k)** Representative coronal sections of layer-specific RV tracing in which starter cells

lack GluN1. Scale bars represent 200 μm. **(f, i, l)** Starter cells are mostly restricted to the defined layer. **(g, j, m)** Comparisons of the patterns of input to control (same as data in Fig. 1) versus GluN1-lacking starter cells (L2/3 SCs: 18±10, inputs: 564±117, n=4 mice; L5 SCs: 152±64, inputs: 4,447±1559, n=6 mice L6→L5, p=0.006; L6 SCs: 146±26, inputs: 1,583±348, n=7 mice, L6→L6 p=0.002). * denotes significant p-values from Student's t-test (c) or multiple t-tests with Holm-Sidak correction for multiple comparisons (α=0.05) (g, j, m). Summary statistics presented as mean±SEM. See Supplementary Table 4 for numerical values. See Supplementary Table 6 for test results and p-values.

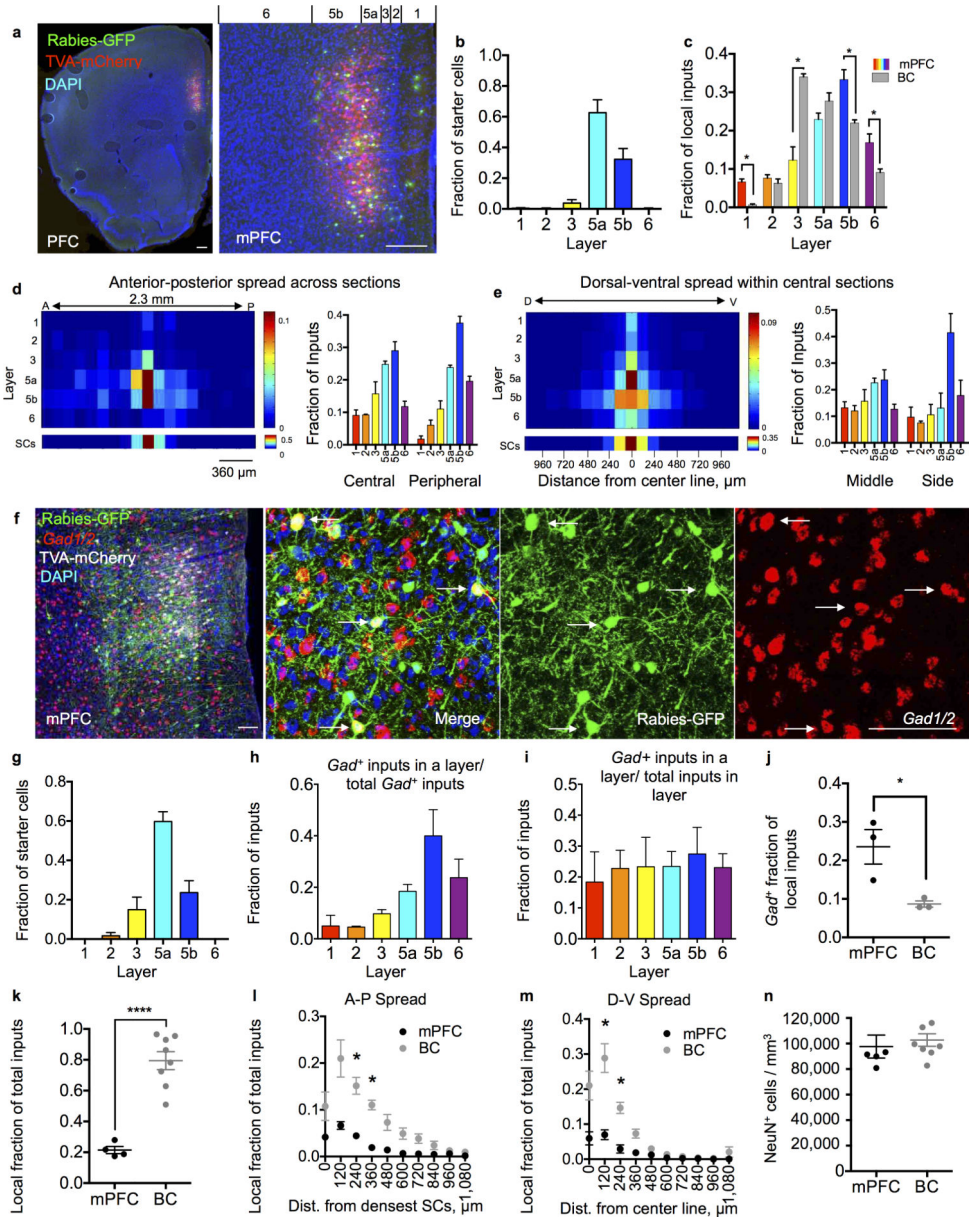

Figure 6.

Local input to mPFC L5. **(a)** Low (left) and high (right) magnification example images of tracing from L5 mPFC neurons. Scale bar represents 200 µm. **(b)** Fraction of starter cells by layer. **(c)** Fraction of local inputs by layer (colored, SCs: 114±33, total inputs: 2,641±664, n=4 mice) in comparison with barrel cortex (BC, grey, n=8 mice). **(d, e)** Left, heat maps of distribution of starter cells (SCs, lower panel) and inputs (upper panel) in each layer along the (**d**) A–P or(**e**) D–V axis. Colors represent fraction of total mPFC cells according to the index at right. Bin widths are 120µm. Right, fraction of mPFC inputs in central versus peripheral sections (**d**; n=4 mice) or in middle versus side regions (**e**; n=4 mice). **(f)** Tracing from L5 starter cells with *Gad1/2 in situ* hybridization. Arrows indicate *Gad*$^+$ inputs. Scale bar represents 100 µm. **(g)** Fraction of starter cells by layer (n=3 mice). **(h)** Fraction of total *Gad*$^+$ cells by layer (n=3 mice). **(i)** *Gad*$^+$ fraction of total inputs in each layer (n=3 mice). **(j)**

Comparison of *Gad*$^{+}$ fraction of local inputs to L5 mPFC versus L5 BC (mPFC: 0.24±0.04, n=3 mice; BC: 0.09±0.008, n=3 mice; p=0.03, Student's t-test). **(k)** Comparison of the local fraction of total inputs to mPFC and BC L5 (mPFC: 0.21±0.02, n=4 mice; BC: 0.79±0.6, n=8 mice; $p=5.14\times10^{-5}$, Student's t-test). **(l)** Spread of local inputs along the A–P axis within mPFC (n=4 mice) or BC (n=8 mice), presented as fraction of total inputs. **(m)** Spread of local inputs along the D–V axis within mPFC (n=4 mice) or BC (n=8 mice), presented as fraction of total inputs. **(n)** Quantification of cell density based on NeuN staining (mPFC: 97,633±9010 cells/mm^3, n=5 sections from 2 mice; BC: 102,760±4876 cells/mm^3, n=8 sections from 3 mice; p=0.59, Student's t-test). * denotes significant p-values from Student's t-tests (**j, k, n**) or multiple t-tests with Holm-Sidak correction for multiple comparisons (α=0.05) (**c, l, m**). Summary statistics presented as mean±SEM. See Supplementary Table 5 for numerical values. See Supplementary Table 6 for test results and p-values.

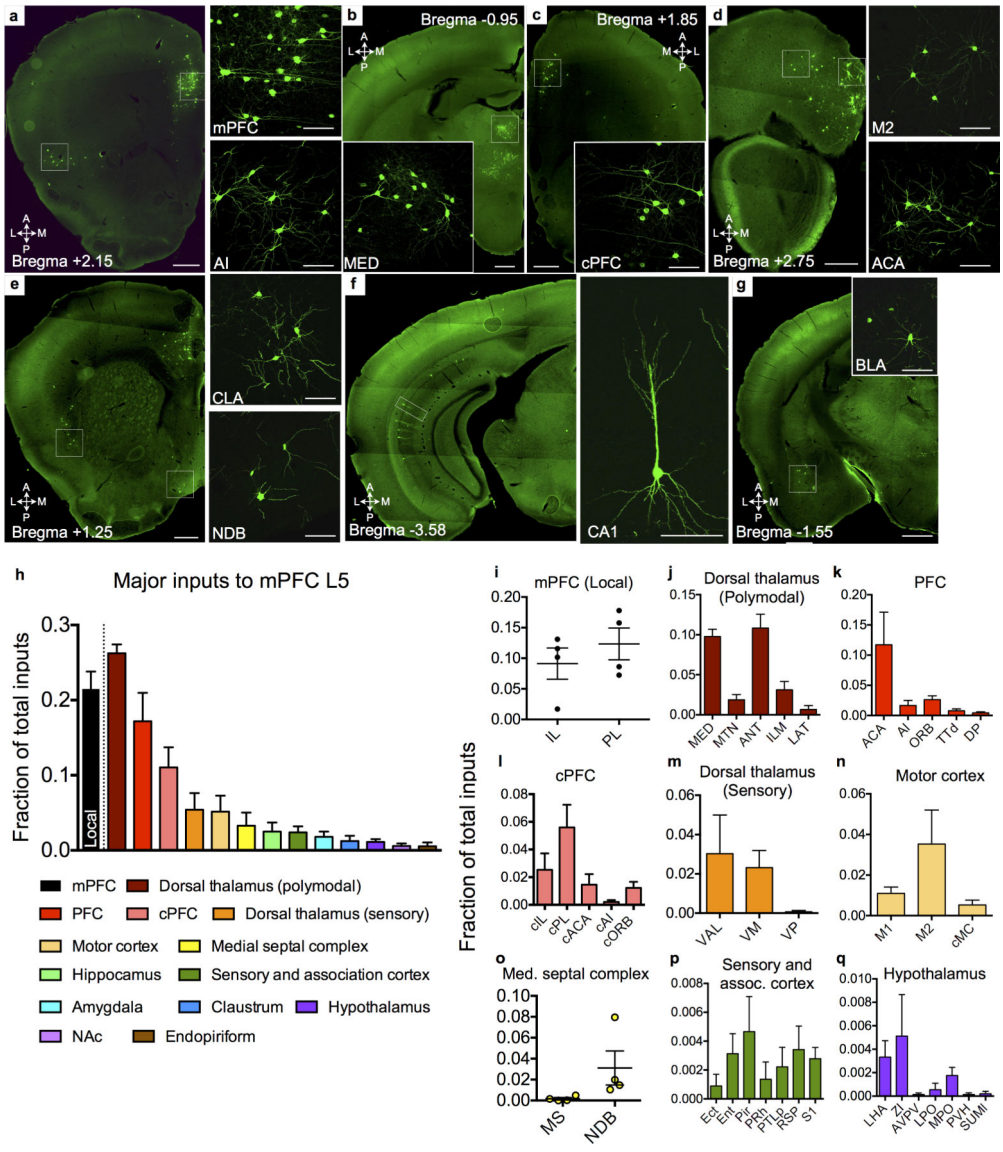

Figure 7.

Long-range input to mPFC L5. **(a–g)** Example images of long-range inputs to L5 mPFC. **(h)** Quantification of major inputs to L5 mPFC (n=4 mice). **(i–q)** Detailed quantification of subregional inputs to mPFC L5 (n=4 mice). Abbreviations not mentioned in text: AVPV, anteroventral periventricular nucleus; Ect, ectorhinal cortex; Ent, entorhinal cortex; LHA, lateral hypothalamic area; LPO, lateral preoptic area; MPO, medial preoptic area; MS, medial septum; NDB, nucleus of the diagonal band; Pir, piriform cortex; PRh, perirhinal cortex; PTLp, posterior parietal association area; PVH, paraventricular hypothalamic nucleus; RSP, retrosplenial cortex; SUMl, supramammillary nucleus, lateral part; ZI, zona inserta. Scale bars represent 500 μm (hemisection images) or 100 μm (zoomed images).

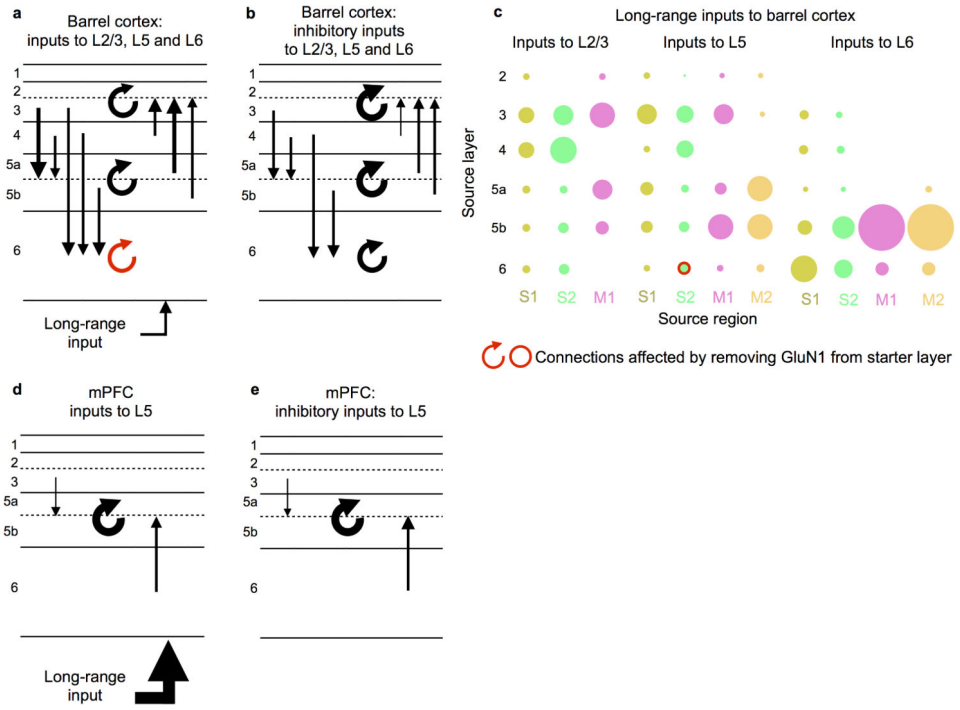

Figure 8.

Summary of major findings. **(a)** Summary of major connections in barrel cortex. **(b)** Summary of major inhibitory connections in barrel cortex. **(c)** Summary of laminar analysis of long-range inputs to barrel cortex L2/3, L5 and L6. **(d)** Summary of major connections in mPFC. **(e)** Summary of major inhibitory connections in mPFC. Arrow thickness in **a, b, d, e**, and circle diameter in **c** correspond to strength of fractional inputs. Only inputs that consist of more than 10% of total inputs to a given layer are represented by arrows. Dotted lines between L2 and L3, as well as L5a and L5b, indicate that while our experiments distinguish the input from these layers (arrows leaving from the middle of these layers), we treat them collectively as recipient of inputs (arrows pointing to the dotted lines).